IonoSeis: A Package to Model Coseismic Ionospheric Disturbances

Thomas Mikesell, Lucie M Rolland, Rebekah Lee, Florian Zedek, Pierdavide Coisson, Jean-Xavier Dessa

To cite this version:

Thomas Mikesell, Lucie M Rolland, Rebekah Lee, Florian Zedek, Pierdavide Coisson, et al.. IonoSeis: A Package to Model Coseismic Ionospheric Disturbances. Atmosphere, 2019, 10 (8), pp.443. 10.3390/atmos10080443 . hal-02373837 *atmosphere*

Article

IonoSeis: A Package to Model Coseismic Ionospheric Disturbances

Thomas Dylan Mikesell [1,*], Lucie M. Rolland [2], Rebekah F. Lee [3,†], Florian Zedek [2], Pierdavide Coïsson [4] and Jean-Xavier Dessa [2]

[1] Environmental Seismology Laboratory, Department of Geosciences, Boise State University, Boise, ID 83725, USA
[2] Institut de recherche pour le Développement, Géoazur, Centre National de la Recherche Scientifique, Observatoire de la Côte d'Azur, Université Côte d'Azur, Sophia Anitpolis, 06560 Valbonne, France
[3] Engineer Research and Development Center, US Army Corps of Engineers, Vicksburg, MS 39180, USA
[4] Institut de physique du globe de Paris, Centre National de la Recherche Scientifique, Université de Paris, F-75005 Paris, France
* Correspondence: dylanmikesell@boisestate.edu; Tel.: +1-208-426-1404
† Previously at Environmental Seismology Laboratory, Department of Geosciences, Boise State University, Boise, ID 83725, USA.

Received: 4 June 2019; Accepted: 27 July 2019; Published: 1 August 2019

Abstract: We present the framework of the modeling package *IonoSeis*. This software models Global Navigation Satellite System (GNSS) derived slant total electron content (sTEC) perturbations in the ionosphere due to the interaction of the neutral atmosphere and charged particles in the ionosphere. We use a simplified model to couple the neutral particle momentum into the ionosphere and reconstruct time series of sTEC perturbations that match observed data in both arrival time and perturbation shape. We propagate neutral atmosphere disturbances to ionospheric heights using a three-dimensional ray-tracing code in spherical coordinates called Windy Atmospheric Sonic Propagation (WASP3D), which works for a stationary or non-stationary atmospheric models. The source of the atmosphere perturbation can be an earthquake or volcanic eruption; both couple significant amounts of energy into the atmosphere in the frequency range of a few Millihertz. We demonstrate the output of the code by comparing modeled sTEC perturbation data to the observed perturbation recorded at GNSS station BTNG (Bitung, Indonesia) immediately following the 28 September 2018, Sulawesi-Palu earthquake. With this framework, we provide a software to couple the lithosphere, atmosphere, and ionosphere that can be used to study post-seismic ionospherically-derived signals.

Keywords: total electron content, coseismic ionospheric disturbance, earthquake observation

1. Introduction

Predicting the arrival time and amplitude of tsunamis along coastlines around the world is one of the most pressing natural hazard challenges facing today's society. Many places on Earth experience significant ground motion, however 72% of our planet is covered by oceans, where it remains challenging to put seismic instrumentation. Moreover, around 10% of the world's population lives in coastal areas less than 10 m above sea level, while 40% of the world's population lives within 100 km of the coast [1]. Satellite-based remote sensing methods provide a new tool to observe tsunami phenomena in the open ocean, well before they reach the shallow water that leads to destructive waves. These same methods are providing new observations into static co-seismic and post-seismic ground deformation as well, something InSAR currently does at low temporal resolution. While we have recently seen an increased number of tsunami observations using GNSS-derived total electron content signals (e.g., [2]), we have yet to see an accurate and comprehensive modeling framework created that enables real-time tsunami hazard characterization. We present the status of our development efforts for such a system, which is dedicated to rapidly quantify ionospheric perturbations related to these natural hazards.

Disturbances in the ionosphere naturally occur at many different wavelengths. On a planetary scale, Rossby waves result from latitudinal variations in the strength of the Coriolis effect and have wavelengths of 1000s of kilometers [3], while, at smaller scales, acoustic gravity waves propagate at wavelengths of 100–3000 km [4,5]. This phenomenon has been known for many decades [6,7,7–12]. Collectively, any disturbance propagating through the ionosphere is known as a traveling ionospheric disturbance (TID). As these disturbances occur at many different wavelengths, that means they also occur at many different periods. Aside from the well-known seasonal and diurnal variations, internal gravity waves, particle precipitation, and ultra-low frequency (ULF) waves also perturb the ionosphere (e.g., [13] and the references therein).

These disturbances disrupt signals in global navigation space system (GNSS) communication. This disruption to GNSS by ionospheric disturbances is a result of the cumulative effects of the total electron content (TEC) along the satellite-receiver line of sight (LOS). GNSS positioning automatically corrects these disruptions using two frequencies. Importantly to this study, Calais and Minster [14] outlined a method to obtain the TEC time series from GNSS data. This trans-ionospheric method derives from the difference of propagation delay between signals emitted by GNSS satellites on two distinct radio frequencies registered by dual-frequency GNSS receivers and provides a mechanism to study the time-history of TEC in the ionosphere layer of not only Earth, but potentially other planetary bodies that contain an ionosphere.

Since the mid-1990s, new applications, for which the GNSS system was not originally designed, have been proposed and developed. For instance, sounding of the atmosphere for troposphere water content [15] or for aerosols in eruptive plumes [16] are now standard uses. More related to this study, global networks of high-frequency GNSS stations provide very dense measurements of TEC, making it possible to invert for the 2D and 3D structure of the ionosphere (e.g., [17]). Over the last decade, researchers around the world have begun analyzing TEC time series to study the source mechanisms and time-histories of acoustic and infra-gravity waves in the atmosphere. In this paper, we focus on a singular application: earthquakes and the acoustic energy coupled from the lithosphere into the atmosphere, which eventually leads to perturbations in the electron density of the ionosphere.

Acoustic waves in the atmosphere associated with TIDs are common and can be caused by a variety of sources, including volcanic eruptions [18], earthquakes [19–21], tsunamis [22], large storms [5,23], solar flares [23], meteorite impacts [23], interplanetary shocks [24], and human-caused sources such as explosions [25] and rocket launches [26] (see [23,27] for comprehensive lists). There is now compelling evidence that the ionosphere is sufficiently affected by earthquake-related ground motion and tsunami waves, the latter of which can be tracked with TEC [28,29].

In this paper, we present a modeling package for acoustic sources derived from coupling of the solid or oceanic part of Earth into the atmosphere. We focus on so-called coseismic ionospheric disturbances (CIDs, e.g., [19]). These are TIDs specifically related to seismic sources. Three classes of CID sources are common in the literature:

1. the direct acoustic wave from the uplift, subsidence, or horizontal motion at the earthquake source (e.g., [19,30–32]);
2. Rayleigh-coupled acoustic waves (e.g., [33]); and
3. internal gravity waves created by mega earthquakes (e.g., [34]).

In all cases, wave energy from a source in the solid-Earth or ocean couples into the atmosphere to create propagating acoustic waves. These acoustic waves travel through the atmosphere and couple into the ionosphere to produce local perturbations in the electron density.

We are currently working to improve our ability to model the GNSS-derived TEC response to acoustic and infra-gravity wave disturbances sourced from Earth's surface and the atmosphere. The most successful attempts to model near-source earthquakes or volcano-induced ionospheric disturbances have been based on acoustic ray tracing combined with an atmosphere–ionosphere coupling model. Thus, over the past few years, we have been developing the software package *IonoSeis* to model CIDs systematically registered with GNSS receivers following the occurrence of shallow earthquakes. *IonoSeis* combines existing and original pieces of code into a single package to rapidly model the electron density from 100 to 500 km altitude and computes TEC signals. We are able to rapidly model this entire process, albeit an approximation to full physics, from the coupling into the atmosphere, propagation to the ionosphere, and coupling in the ionosphere to perturb the electron density. This software does not model nonlinear wave breaking effects or resonance in the lower atmosphere due to refraction. At present, this code only models the direct wave caused by the source uplift. Some effects (e.g., dissipation) are taken into account and how this is done is presented in the following sections. Finally, we discuss the parts of the package that we plan to improve in the future and present an example case study from the 2018 Sulawesi tsunamigenic earthquake.

The main objective of this paper is to present our current modeling framework and discuss the obstacles of this multi-physics problem. We suspect that, once the scientific community has a robust modeling code, we can begin to better characterize the relationship between the earthquake rupture and observed TEC perturbations. Observational studies have already demonstrated (e.g., [21]) the potential relationships between earthquake parameters and TEC amplitude beyond vertical uplift (i.e., dip-slip motion). However, because of the complex coupling among the neutral atmosphere, the ionosphere, and the TEC measurement method (e.g., line-of-sight integration), the amplitude of observed TEC can vary due to myriad processes, and there is not a simple (linear) relationship between the surface motion of the solid Earth or ocean and the amplitude of observed TEC perturbations. Recent studies have used *IonoSeis* to study complex earthquake sources (e.g., [35,36]), and hence a detailed publication of this software is warranted.

2. Materials and Methods

The ionospheric signal that we observe with dual-frequency GNSS communications is the slant total electron content (sTEC) [14]. sTEC is defined as the path integral from a moving satellite to a (static) receiver on Earth's surface:

$$sTEC(t) = \int_{Receiver}^{Satellite} N_e(\vec{r}, t) d\vec{r}, \tag{1}$$

where $N_e(\vec{r}, t)$ is the electron density of Earth's atmosphere (e.g., [37]). The limits of the integrand are the location of the *Satellite* and *Receiver*, respectively, in an Earth-centered, Earth-fixed (ECEF) coordinate system. The implementation of the LOS integration is provided in Appendix A. In the following subsections, we discuss how we compute $N_e(\vec{r}, t)$ within our modeling framework such that we can compute TEC using Equation (1). We also describe how we extract sTEC from actual GNSS data.

2.1. sTEC Observation Data

The sTEC measurement differs from another TEC measurement, which is called vertical TEC (vTEC) (e.g., [38]). The unit of measurement for TEC is the total electron content unit (1 TECU = 10^{16} electrons/m^2). We can extract the biased sTEC time series from the phase differences of the two GNSS carrier frequencies (e.g., [31,39,40]). The following formula is used to obtain sTEC from the carrier phases,

$$sTEC(t) = \frac{1}{40.3} \times \left(\frac{f_1^2 \times f_2^2}{f_1^2 - f_2^2} \right) \left(L_1(t) \times \lambda_1 - L_2(t) \times \lambda_2 \right), \tag{2}$$

where f_1 and f_2 are carrier wave frequencies (1.2 GHz and 1.5 GHz, respectively), λ_1 and λ_2 are the corresponding wavelengths, and L_1 and L_2 are the carrier phases.

2.2. The Electron Density Model

To model the observed sTEC, we need to model the dynamic electron density in the ionosphere, which is a multi-physics problem. The electron density depends on altitude, local time, and a variety of other non-stationary processes. In this study, we define $N_e(\vec{r}, t)$ as the sum of the background density (N_{e0}) and a local perturbation (δN_e) due to a passing acoustic wave propagating through the atmosphere. In this way, we split the integral in Equation (1) into two parts:

$$sTEC(t) = \underbrace{\int_{Receiver}^{Satellite} N_{e0}(\vec{r}, t) d\vec{r}}_{background\ TEC} + \underbrace{\int_{Receiver}^{Satellite} \delta N_e(\vec{r}, t) d\vec{r}}_{perturbation\ TEC}. \tag{3}$$

The modeling of the ionosphere is thus divided into two parts:

1. modeling the background electron density (N_{e0}); and
2. modeling local perturbations (δN_e) due to transient phenomena.

In this particular study, we call this second part the coseismic ionospheric perturbation (CIP). By computing sTEC using Equation (3), we provide the user with both the background sTEC and the perturbation sTEC time series. The user can add the two time series together to estimate the complete sTEC with time. We now work backwards—from the ionosphere to the ground surface—to present the framework of how we calculate the CIP, beginning first with a description of how the background electron density is derived.

2.2.1. The Background Ionosphere

There are many models that exist for the Earth's background ionosphere. These models are based on a number of different physical assumptions and lead to slightly different time-dependent values. Solar radiation strongly impacts the atmosphere temperature and molecular composition [41] used to derive the parameters of the propagation medium (i.e., sound speed and density); therefore, the local time and geographic location are important to all ionosphere models. To generate the ionosphere model in *IonoSeis*, we use the International Reference Ionosphere (IRI2016) model (e.g., http://irimodel.org [42]) to compute the background electron density (N_{e0}). Using the IRI2016 package, we generate a three-dimensional grid in the atmosphere directly above the solid Earth or ocean surface. This grid exists from 100 to 500 km altitude and can extend laterally to about 700 km from the earthquake/tsunami epicenter. The 3D grid spacing in the vertical direction is 5 km, and the horizontal spacing is 40 km. These spacings can be varied by the user, at the cost of more or less computation time. For horizontal wavelengths around 100s km, the horizontal spacing of 40 km provides 3–4 points per wavelength. In the current implementation, the grid is centered directly above the known earthquake source location (i.e., the epicenter). It is important to note that not only does the electron density vary significantly with altitude, it also varies with latitude, longitude, and local time. Once the background electron density is known, we can compute the CIP.

2.2.2. The Coseismic Ionospheric Perturbation

We obtain the CIP following a simplified neutral-plasma coupling scheme proposed by Rolland et al. [33]. In essence, we project the neutral particle motion $\vec{v}_n(\vec{r}, t)$ into the direction of the local geomagnetic field $\vec{B}(\vec{r})$ following Hooke [12] to create the ionized particle motion field $\vec{v}_i(\vec{r}, t)$:

$$\vec{v}_i(\vec{r}, t) = \left[\vec{v}_n(\vec{r}, t) \cdot \hat{B}(\vec{r})\right] \hat{B}(\vec{r}). \tag{4}$$

Equation (4) is derived from [43], with $\hat{B}$ the magnetic field unit vector (see [33] for the complete derivation of Equation (4)). In this formulation, we neglect other sources of plasma motion (e.g., equatorial spread F or other disturbance electric fields from storms (Chapter 11 in [4])) that occur on the same time scales as CIDs. The 3D electron density perturbation δN_e is computed by integrating the linearized electron density continuity equation over time:

$$\delta N_e(\vec{r}, t) = \int_0^t \nabla \cdot [N_{e0}(\vec{r})\vec{v}_i(\vec{r}, t)]\, dt. \tag{5}$$

In this formulation, we assume loss and production terms due to photoionization and chemical reactions are steady and equal (e.g., [13]) such that we can neglect them. We also assume that perturbations are small compared to the background electron density N_{e0}. The divergence term in Equation (5) is computed using a centered finite difference (Appendix B). We compute the full 3D divergence because initial tests demonstrated that the variation in lateral electron density led to significant differences in TEC during the LOS integration [44]. This is in contrast to other studies which sometimes approximate this term using only the radial (or local vertical) component of the divergence (e.g., [45]), which can be valid in the far-field approximation, where an acoustic wave can be considered a plane wave.

2.2.3. The Geomagnetic Field

From *IRI2016*, we obtain the geomagnetic field inclination and declination on the same 3D grid as the ionosphere model. These parameters come from the International Geomagnetic Reference Field (IGRF) model [46]. The significance of the geomagnetic field in Equation (4) can be observed in the so-called ionospheric coupling coefficient [25]. The coupling coefficient (α) is defined as

$$\alpha = \vec{k} \cdot \hat{B}, \tag{6}$$

where $\vec{k}$ is the wave vector of $\vec{v}_n(\vec{r}, t)$ (i.e., the neutral particle velocity). The coupling coefficient is therefore the projection of the neutral particle velocity onto the geomagnetic field vector [12]. The ion velocity $(\vec{v}_i)$ induced by the neutral particle motion is largely proportional to α (e.g., Figures 12 and 13 in [33]), which describes how the neutral particles transfer momentum into the ionized particles. As evident in Equation (4), the ionized particles only transfer momentum in the direction of the local geomagnetic field, so only a portion of the momentum is transferred from the neutral particles to the ionized particles.

2.3. The Neutral Particle Velocity

To compute either the coupling coefficient (α) or the ionized particle velocity $(\vec{v}_i)$, we need to know the incident neutral particle velocity, which comes from the acoustic wave perturbation. We model the acoustic source as a purely compressional point source located at the Earth's surface. We propagate the resulting acoustic perturbation using three-dimensional Hamiltonian acoustic ray tracing in a 1D (stratified) atmospheric model, where we shoot rays at many azimuths and many take-off angles in order to sample the entire 3D ionosphere grid. There are multiple approaches to numerically compute $\vec{v}_n(\vec{r}, t)$ (e.g., [33,47–50]), but we use ray tracing in *IonoSeis;* specifically, we use the *WASP3D* package from [51], which operates in a spherical coordinate system with a one-dimensional layered atmosphere and was previously used for infrasound modeling in a heterogeneous atmosphere (e.g., [52]). This package solves the linearized hydrodynamic equations for a compressible fluid in the high-frequency approximation. We do not model acoustic resonances due to multiple bounces in the low atmosphere waveguide. We also do not currently model lower frequency gravity waves. We only model the acoustic wave with *IonoSeis*.

From the WASP3D ray tracing, we determine the arrival time (t_w), wave vector $(\vec{k}_w)$, and an amplification factor (A_w) related to geometrical spreading and kinetic energy conservation. Note that

WASP3D-derived variables contain the subscript w. After computing these parameters along rays propagated throughout the 3D model, the parameters (t_w, $\vec{k}_w$, and A_w) are linearly interpolated to the 3D ionosphere grid such that we can write the neutral particle velocity as a function of space and time:

$$\vec{v}_n(\vec{r},t) = v(\vec{r},t)A_w(\vec{r})\vec{k}_w(\vec{r},t), \tag{7}$$

where v defines the time-history of acoustic wave amplitude (i.e., the source-time function) and $\vec{k}_w$ defines the direction of propagation. This approach follows from ([31], Equation (2)), where we combine a source-time function (STF) with the information from the acoustic ray tracing. In essence, we use the arrival time information to build an impulse response and then convolve the impulse response with a STF. We model the STF as a co-seismic acoustic shock-wave taking the form of a bipolar pulse following [18,25,30]. The STF we use in *IonoSeis* is thus the first derivative of a Gaussian pulse (i.e., an N-wave)

$$v(\vec{r},t) = A_z(\vec{r})\frac{A_o\sqrt{2}}{\sigma^{3/2}\pi^{1/4}}\,(t-t_0)\,e^{-\frac{(t-t_0)^2}{\sigma^2}}, \tag{8}$$

where t_0 is the time of maximum particle motion; σ is the pulse width in seconds; A_o is the initial amplitude factor, which scales the amount of energy injected in the atmosphere from the point source [18]; and A_z is an amplitude factor that describes how the phase and amplitude are affected by frequency-dependent viscous and thermal losses with altitude (Appendix C). We choose this source model, not because it completely describes the true physics, but because it approximates the observed waveforms well (e.g., [18]), and will allow us to make quantitative comparisons between modeled and observed data in future studies.

We currently include propagation effects not modeled by WASP3D in an ad-hoc way. First, following the approach proposed by Dautermann et al. [18], we parameterize the broadening of the pulse, which is due to dispersion, by adjusting σ:

$$\sigma(\vec{r},t) = bt_w, \tag{9}$$

where b is a scale factor so that the pulse width increases with propagation time. Second, we compute the viscous attenuation effects on the amplitude for a 10 mHz monochromatic wave following Garcia et al. [53]; this frequency is the central frequency of the signal we intend to model. Using a normal mode analysis, Lognonné et al. [54] determined that certain frequencies sufficiently couple from the solid Earth into the atmosphere, and hence we choose a center frequency in the range of frequencies related to propagating acoustic waves. Finally, the term A_z varies only in altitude (Appendix C) and is applied in addition to the geometrical spreading and kinetic energy conservation term A_w.

3. Results

The *IonoSeis* package is currently implemented with a number of Fortran90 and MATLAB routines. The following steps are required to generate TEC time series.

1. Create the model domain—build a 3D grid in the atmosphere that contains background electron density and geomagnetic field parameters → save to a NetCDF file.
2. For a given epicenter location, run WASP3D over many rays (azimuths and take-off angles) to model the arrival time, the amplitude, and the wavevector of the acoustic wave.
3. Interpolate the ray parameters to the atmosphere grid → create a single NetCDF file with all necessary parameters.
4. Solve Equation (5) using time integration—create a NetCDF file with the electron density perturbations (δN_e) at each time step.
5. Perform LOS integration for a given receiver and satellite pair—create SAC formatted data files that contain the LOS integration for both the background TEC and the CIP TEC (i.e., Equation (3)).

The user can select the time step used in time-integration (Step 3); this is usually 1 or 5 s. It is possible to interpolate or decimate the numerical data to match observed data (e.g., 30 s GNSS data are common), but nothing for this is yet implemented in *IonoSeis*. The user can set parameters at each step in a corresponding BASH script that is used to run each step (Figure 1). Below, we demonstrate the code capabilities with a dataset from the recent Sulawesi earthquake in Indonesia.

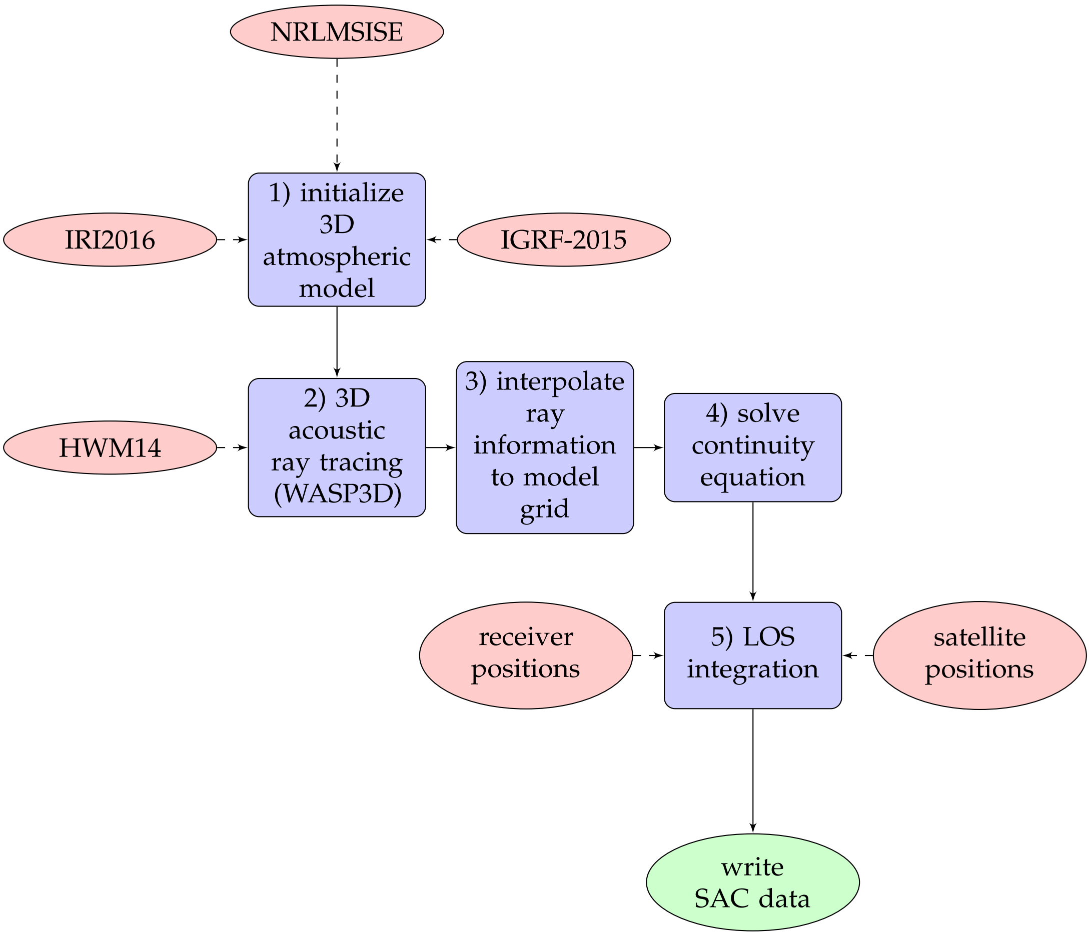

Figure 1. Flow diagram for the *IonoSeis* modeling framework. The SAC data format is used to store the sTEC time series. NetCDF files are used to store grid information between each step (blue blocks). Red ovals indicate model inputs, and blue boxes indicate individual steps that each have their own BASH script with input parameters for that step.

Example: 2018 Sulawesi Earthquakes

To demonstrate the current capabilities of the *IonoSeis* package, we present a comparison of observed and modeled sTEC data for the shallow (20 km depth) M_w 7.5 event that occurred on 28 September 2018, Sulawesi, Indonesia. This sequence consisted of two cascading events (M_w 6.1 and M_w 7.5 earthquakes) that struck the city of Palu on the Indonesian island of Sulawesi [55]. A remarkable and rare feature is the fact that the rupture propagated at super-shear speed [56]. There was liquefaction, landslides, and a near-field tsunami as a result. We show the location of the earthquake epicenter in Figure 2 with the beach ball diagram that indicates this was a dip-slip earthquake.

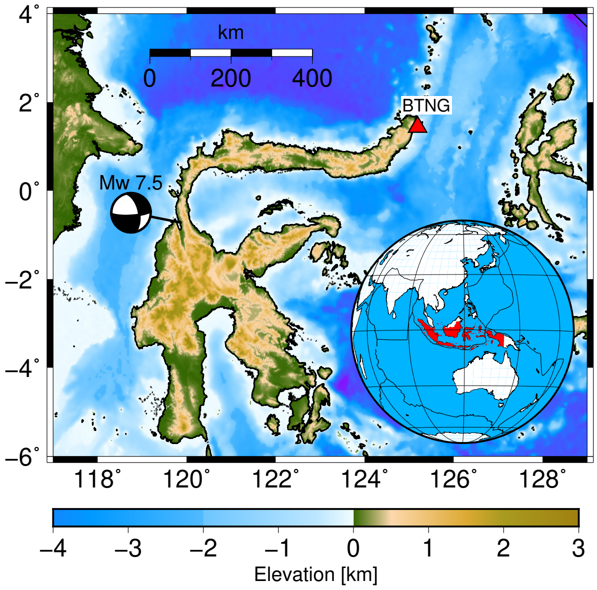

Figure 2. Map of the Sulawesi region and the GNSS receiver used in this study. Receiver BTNG (Bitung, Indonesia) is the only station within 600 km of the epicenter that has open-access data. The beach ball describes the earthquake moment tensor, which indicates dip-slip motion along this fault. Inset shows Indonesia in red, centered on the Sulawesi M_w 7.5 epicenter.

We downloaded the Rinex file for GNSS receiver BTNG from UNAVCO. This is the only dual-band GNSS receiver within 600 km of the epicenter available at UNAVCO. From this file, we extracted the sTEC signal using the TEQC program from UNAVCO. We applied a linear detrend from 0 to 1 h after the event to remove the satellite motion contribution to the sTEC (Figure 3a). We then applied a zero-phase second-order IIR Butterworth filter from 2 to 13 mHz [57] (Figure 3b). This station has a max sTEC perturbation amplitude around 0.1 TECU (Figure 3b), which is relatively strong. Weak CID recordings can be related to a number of factors. For instance, the geomagnetic field plays a significant role in both the amplitude and polarity of TEC observations [31], as well as the observation geometry (e.g., [58]). In particular, the amplitude largely depends on the geomagnetic latitude of the event, the GNSS receiver location, and the satellite look angle [32,33]. The signal from this CID (black line) is above the background noise; therefore, we model this sTEC perturbation using the *IonoSeis* package.

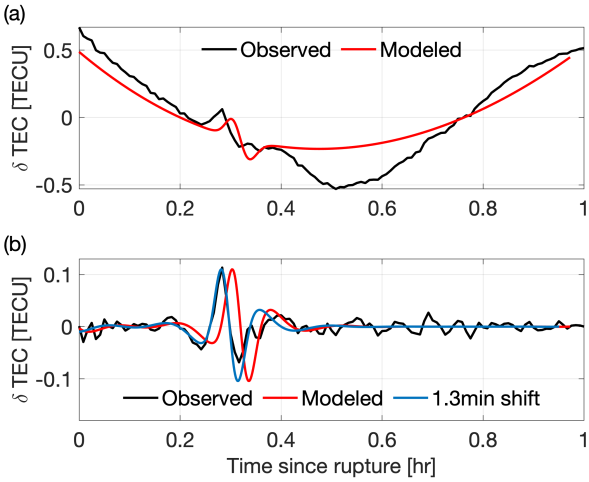

Figure 3. Observed and modeled sTEC at station BTNG for GPS satellite 21: (**a**) sTEC after linear detrend from 0 to 1 h; and (**b**) perturbation signal after bandpass filtering (**a**) from 2 to 13 mHz, including the modeled time series after a 1.3 min advanced.

Figure 4 shows the local sound speed profile with height at the time of rupture. For the atmospheric conditions at the Sulawesi earthquake time and epicenter, the amplification factor reaches 1.23×10^5 at ∼220 km of altitude before rapidly decreasing due to the filtering properties of the atmosphere [22] and the decrease in density.

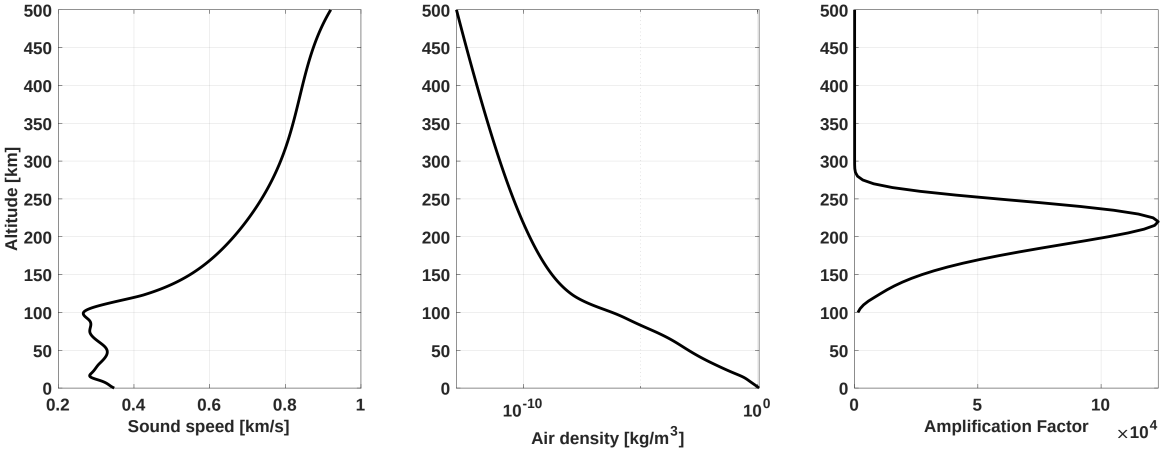

Figure 4. (**Left**) Atmospheric sound speed profile computed from the NRLMSISE-00 model [59] on 28 September 2018 at 10:02:43 UTC (18:02 Mean Local Time) above the epicenter (0.256S/119.846E); (**Center**) air density profile; and (**Right**) atmospheric amplification factor.

The background electron density for this time was modeled using a geomagnetic index Kp of 0.7 (very low geomagnetic activity) and a solar radio flux at 10.7 cm (F10.7 Index) of 69.4, with the 81-day average (±40 days) equal to 69.1. The F10.7 index tracks solar flare activity and is a proxy for the Extreme UltraViolet (EUV) emissions that impact the ionosphere. This index is measured daily at Penticton, Canada [60], and it should be noted that, if *IonoSeis* were to be used in real-time, we would need a predicted estimate of this index, as IRI2016 updates that daily data only every six months. The geomagnetic field, also modeled in 3D, has an inclination angle at the epicenter of -12.6°.

To match the observed sTEC perturbation, the electron density perturbation (δN_e) was scaled by an amplitude factor (A_o) of 1.2×10^3 and the scaling coefficient b was set to 0.5, which is similar to previous studies (e.g., [31,35]). The value of b is related to the source uplift region, but we do not yet have a physics-based model that relates this term to the actual ground displacement. This is an area of future research. After linearly detrending the synthetic data from 0 to 1 h after rupture, we observe that the sTEC matches the observed data well in terms of overall structure (Figure 3a), but less so after the CID arrives, which may be related to ion recombination effects (i.e., the decrease in sTEC around 0.5 h). After filtering the synthetic data within the same frequency band as the observed sTEC, we observed that the waveform shapes also match well; however, there is a small delay in the arrival time of the synthetic CID (Figure 3b).

In general, the modeled sTEC perturbation matches the observed sTEC perturbation well in terms of shape and arrival time. From this, we infer that the observed TID is in fact a CID triggered by the epicentral uplift zone, creating an acoustic shock-wave taking the form of a compression-rarefaction pulse. The N-shape is conserved due to the maximum neutral-ionosphere coupling configuration and favorable observation geometry as reported by Heki and Ping [19] and Rolland et al. [31]. A closer look shows that the rarefaction phase is significantly smaller in the observed perturbation than in the modeled waveform. This discrepancy can come from nonlinear effects not taken into account during the neutral-ionosphere coupling step and also from nonlinear propagation of the acoustic wave in the atmosphere. Further investigation is needed to decipher how the different parts of the model contribute to the final waveform.

To demonstrate the geometry of the line-of-sight integration, we plot the background electron density and perturbation in map-view in Figure 5a,b, respectively. We observed variations in the background density related to the geomagnetic equator, and we observed a change in polarity of the perturbation between northward and southward propagation related to the neutral-plasma coupling model (e.g., Equation (6)). We also observed a larger perturbation amplitude in the southward propagating pulse.

We next present in Figure5c,d the vertical cross sections along the solid black lines in Figure 5a,b. These vertical cross sections are along the plane that lies in the satellite-receiver line-of-sight path. This is the path along which the integration in Equation (1) occurs. The blue triangle identifies the ground location of the GNSS station BTNG. The cyan dot identifies the IPP; note that the IPP here is for visualization purposes only—to show the altitude of the horizontal slice and the trajectory of the LOS. The IPP is placed at an altitude of 300 km, which lies directly above the zone of maximum amplification (e.g., Figure 4). In reality, the IPP location is moving through space and the LOS integration actually extends to the satellite at 20,200 km altitude. At this altitude and time after the rupture, the perturbation is moving almost entirely horizontally from left to right (Figure 5d) and the LOS integration intersects the perturbation obliquely (Figure 5b).

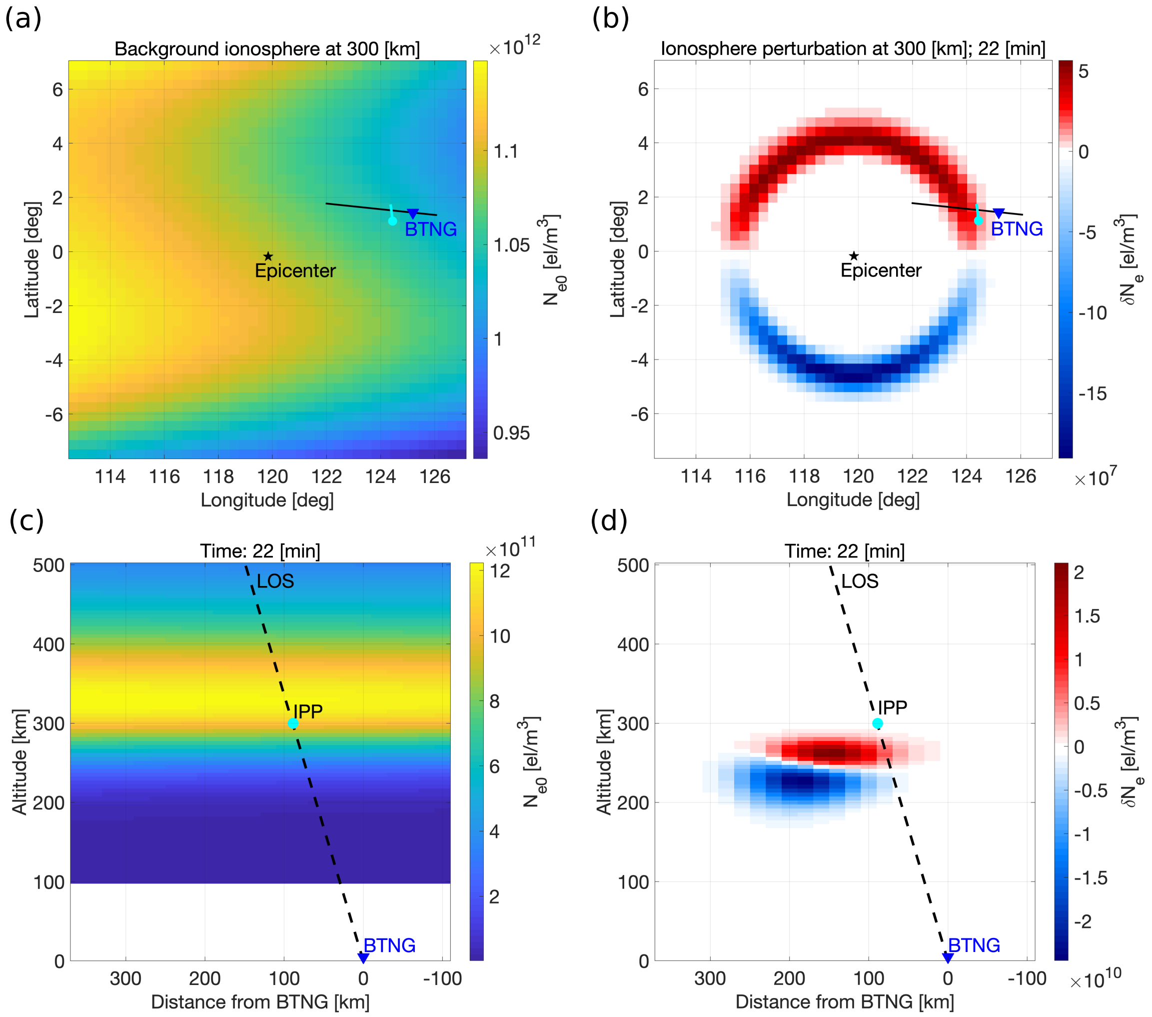

Figure 5. Background electron density (**a**); and electron density perturbation 22 min after rupture (**b**) at an altitude of 300 km. The cyan line shows the track of the IPP at 300 km, with the circle indicating the end of the track 3500 s after the rupture. Blue triangle is the GNSS station BNTG at the ground surface. The solid black line indicates the vertical plane shown in (**c**,**d**). Background electron density (**c**); and electron density perturbation (**d**) in a vertical plane along the satellite-receiver LOS at 22 min (GPS satellite 21).

4. Discussion

The *IonoSeis* software package can be used to rapidly model sTEC due to a point source on Earth's surface. The code has now been used in a few studies (e.g., [35,36]), and we continue to make improvements, including reducing the approximations made in the physics. As is evidenced by the modeled data in Figure 3, the synthetic model predicts the electron density perturbations 1.3 min after the observed perturbation (Figure 3). This has been noted previously (i.e., [35]), and research is underway to determine the cause of this arrival time discrepancy. This delay increases with distance between the event epicenter and the ionospheric sounding point along the LOS. It is possible that this delay is due to an inaccurate velocity model or other physics at high altitudes, which rays must pass through to make it to epicentral distances of 500 km or more. We note that other GNSS stations were present in the region, but they were at distances greater than 900 km. We currently cannot model ionospheric perturbations this far away until we improve the sampling of the atmosphere by shooting rays at nonlinear intervals. At the moment, the WASP3D code shoots rays over a linearly defined range. There are many areas where this software can be improved, but it is now at a stage that it is ready to be shared with the community so that others can start to study CID phenomena.

5. Conclusions

We present the framework of a modeling code called *IonoSeis*. This software enables the computation of GNSS-derived sTEC perturbations due to earthquakes and tsunamis (i.e., CIDs). We demonstrate that the code reproduces the sTEC signal recorded at GNSS station BTNG to within 1.3 min for the M_w 7.5 2018 Sulawesi, Indonesia event. The method is based on ray-tracing and a simplified coupling of the neutral atmosphere to the ionosphere. In an ad-hoc way, the modeling accounts for viscous dissipation and dispersion due to propagation in the rarefied atmosphere at ionospheric heights. The package accurately honors the geometry of the moving satellite-receiver line-of-sight integration. This new software package can be used in the future to study processes related acoustic coupling from the lithosphere into the atmosphere, which can eventually perturb the ionosphere. Thus, there exists the potential to study not only earthquakes, but also tsunamis and other phenomena with this new software package.

Author Contributions: All authors helped develop the IonoSeis package. The following specific contributions were made: conceptualization, T.D.M. and L.M.R.; methodology, T.D.M. and L.M.R.; software, all; validation, T.D.M., L.M.R., R.F.L. and F.Z.; formal analysis, R.F.L.; investigation, all; resources, T.D.M.; data curation, T.D.M.; writing—original draft preparation, T.D.M.; writing—review and editing, all; visualization, T.D.M.; supervision, T.D.M. and L.M.R.; and project administration, T.D.M. and L.M.R.

Funding: L.M.R. and F.Z. acknowledge support for this research from the French Space Agency CNES (Centre National d'Etudes Spatiales) and Université Côte d'Azur Investissement d'Avenir project funded by ANR (Agence Nationale de la Recherche), reference number ANR-15-IDEX-01.

Acknowledgments: The authors acknowledge two anonymous reviewers who helped improve the quality of this article. The authors thank all contributors to the reference models (IRI2106, IGRF, and HWM14) for providing these open source products to the community. The authors thank David Themens and the ECHAIM project of the Canadian High Arctic Ionospheric Network for providing the F10.7 data and the GFZ German Research Centre for Geosciences for providing Kp index data. This material is based on services provided by the GAGE Facility, operated by UNAVCO, Inc., with support from the National Science Foundation and the National Aeronautics and Space Administration under NSF Cooperative Agreement EAR-1724794. The seismic moment tensor for the Sulawesi-Palu earthquake was provided by the USGS National Earthquake Information Center. This is IPGP contribution no 4057.

Conflicts of Interest: The authors declare no conflict of interest.

Abbreviations

The following abbreviations are used in this manuscript:

GNSS	global navigation space system
IGRF	International Geomagnetic Reference Field
IRI	International Reference Ionosphere
TEC	total electron content
sTEC	slant TEC
vTEC	vertical TEC
TID	traveling ionospheric disturbance
CID	coseismic ionospheric disturbance
LOS	line-of-sight
CIP	coseismic ionosphere perturbation
2D	two-dimensional
3D	three-dimensional
STF	source-time function

Appendix A. Line-of-Sight Integration

The satellite-receiver line-of-sight (LOS) integration presented in Equation (1) requires a few steps to calculate. To model the TEC signal, we need the following information:

1. the receiver location (stationary or non-stationary, e.g., a ground receiver or ship, respectively);
2. the satellite location (non-stationary); and
3. the electron density along the path (i.e., the line-of-sight or LOS).

The first two items in this list are straightforward. The receiver location is known a priori, and the satellite position (from IGS orbits) can be obtained from a number of different locations (e.g., NASA's CDDIS). The accuracy of IGS orbit solutions vary. Users can access:

- ultra-rapid orbits: released at regular intervals four times per day, which includes both observed and predicted orbits;
- rapid orbits: released approximately 17 h after the end of the previous UTC day; and
- final orbits: released on a weekly basis, approximately 13 days after the end of the solution week.

One kilometer accuracy is sufficient in our tests; therefore, approximate positions such as predicted orbits can be used without significant degradation of the results.

The third item in the list (electron density) needs to be interpolated from the 3D atmosphere grid to the LOS. This is done at each altitude in the 3D atmosphere grid. The first step to accomplish this is to convert all latitudes, longitudes, and altitudes to a Cartesian coordinate system. We use an Earth-centered, Earth-fixed (ECEF) system. Then, given the satellite and receiver positions, we interpolate the 3D atmosphere grid (N_{e0} and δN_e) to the LOS intersection at each altitude in the 3D grid. This is achieved using a 2D-spline interpolation at each altitude. We then use trapezoidal integration in 3D space to generate each term in Equation (3). In this way, we construct the sTEC time series. The code supports LOS integration using non-stationary satellites and produces both background ionosphere and perturbation TEC time series. The code outputs SAC formatted data (a common seismology data format) or ASCII text formatted data in TECU.

Appendix B. Divergence in Spherical Coordinates

The divergence of a vector $\vec{W}$ in spherical coordinates is given by

$$\nabla \cdot \vec{W} = \frac{1}{r^2}\frac{\partial\left(r^2 W_r\right)}{\partial r} + \frac{1}{r\sin\theta}\frac{\partial}{\partial\theta}\left(W_\theta \sin\theta\right) + \frac{1}{r\sin\theta}\frac{\partial W_\varphi}{\partial\varphi}, \tag{A1}$$

where W_r is the radial component, W_θ is the colatitude component, and W_φ is the longitudinal component. We compute each term in the equation using centered finite differences for first-order quotients (e.g., $\partial f/\partial r = [f(r+dr,t) - f(r-dr,t)]/2dr$.)

Appendix C. Atmosphere Model

The 1D atmospheric model used in *IonoSeis* is computed at the location of the earthquake during the exact rupture time. The atmospheric model is derived from the empirical, global reference atmospheric model *NRLMSISE-00* [59]. The important parameter going into this model is solar-radio flux at 10.7 cm (i.e., the F107 parameter), which characterizes solar activity. Assuming the sound wave is an adiabatic disturbance and that the atmosphere follows the ideal gas law, the speed of sound is

$$c = (\gamma RT/M)^{1/2}, \tag{A2}$$

where R is the gas constant equal to 8.31432×10^3 J·kmol^{-1}·K^{-1}, M is the molecular weight in kg·kmol^{-1} and T is the ambient temperature in K. It is worth noting that the ray tracing can account for non-stationary atmospheric models and we have integrated the Horizontal Wind Model (HWM14) from [61] into *IonoSeis*. In essence, this leads to an anisotropic sound speed model.

Due to conservation of kinetic energy, the wave amplitude increases as the inverse square root of the air density. This effect is counterbalanced by the viscous dissipation that increases as the density decreases. The modeling used in *IonoSeis* accounts for this amplitude variation for a 10 mHz vertically propagating plane wave after [62].

Absorption

The general form for absorption due to viscosity and thermal conduction is

$$\alpha = \left[\omega^2 / \left(2\rho_o c^3\right)\right] \left[4\mu/3 + \kappa(\gamma - 1)/c_p\right], \tag{A3}$$

where $\omega = 2\pi f$, f is frequency in Hz, ρ_o is the equilibrium density in kg·m^{-3}, c is the speed of sound in m·s^{-1}, μ is the coefficient of dynamic viscosity in kg·m^{-1}·s^{-1}, γ is the ratio of specific heats, κ is the coefficient of thermal conductivity in J·m^{-1}·s^{-1}·K^{-1}, and c_v is the specific heat at constant pressure in J·K^{-1} [63]. The units of α are Np·m^{-1}.

Following Landau and Lifshitz [64], we account for absorption with the addition of an energy dissipation term. In the current version of *IonoSeis*, we account for changes in amplitude in the vertical direction only. We write the dissipation term as $A_z(\vec{r}) = e^{-\alpha \Delta z}$, where Δz is the distance between grid nodes in the vertical direction. This amplitude effect is cumulative and the code should eventually compute this amplitude effect along the actual acoustic ray path. An example of this amplification function is presented in Figure 4, where the peak is between 200 and 250 km at the time of the earthquake rupture.

References

1. United Nations. *Factsheet: People and Oceans*; The Ocean Conference; United Nations: New York, NY, USA, 5–9 June 2017.
2. Rolland, L.M.; Occhipinti, G.; Lognonné, P.; Loevenbruck, A. Ionospheric gravity waves detected offshore Hawaii after tsunamis. *Geophys. Res. Lett.* **2010**, *37*. [CrossRef]
3. Beer, T. *Atmospheric Waves*; Halsted Press Book; Wiley: Hoboken, NJ, USA, 1974.
4. Schunk, R.; Nagy, A. *Ionospheres: Physics, Plasma Physics, and Chemistry*; Cambridge Atmospheric and Space Science Series; Cambridge University Press: Cambridge, UK, 2009.
5. Vadas, S.L.; Crowley, G. Sources of the traveling ionospheric disturbances observed by the ionospheric TIDDBIT sounder near Wallops Island on 30 October 2007. *J. Geophys. Res. Space Phys.* **2010**, *115*, 1–24. [CrossRef]

6. Georges, T.M. Evidence for the influence of atmospheric waves on ionospheric motions. *J. Geophys. Res.* **1967**, *72*, 422. [CrossRef]
7. Hooke, W. Ionospheric irregularities produced by internal atmospheric gravity waves. *J. Atmos. Terr. Phys.* **1968**, *30*, 795–823. [CrossRef]
8. Hooke, W.H. E-region ionospheric irregularities produced by internal atmospheric gravity waves. *Planet. Space Sci.* **1969**, *17*, 749–765. [CrossRef]
9. Georges, T.M.; Hooke, W.H. Wave-induced fluctuations in ionospheric electron content: A model indicating some observational biases. *J. Geophys. Res.* **1970**, *75*, 6295–6308. [CrossRef]
10. Hooke, W.H. Ionospheric response to internal gravity waves: 3. Changes in the densities of the different ion species. *J. Geophys. Res.* **1970**, *75*, 7239–7243. [CrossRef]
11. Hooke, W.H. Ionospheric response to internal gravity waves: 2. Lower F region response. *J. Geophys. Res.* **1970**, *75*, 7229–7238. [CrossRef]
12. Hooke, W.H. The ionospheric response to internal gravity waves: 1. The F2 region response. *J. Geophys. Res.* **1970**, *75*, 5535–5544. [CrossRef]
13. Pilipenko, V.; Belakhovsky, V.; Murr, D.; Fedorov, E.; Engebretson, M. Modulation of total electron content by ULF Pc5 waves. *J. Geophys. Res. Space Phys.* **2014**, *119*, 4358–4369. [CrossRef]
14. Calais, E.; Minster, J.B. GPS detection of ionospheric perturbations following the January 17, 1994, northridge earthquake. *Geophyis. Res. Lett.* **1995**, *22*, 1045–1048. [CrossRef]
15. Bevis, M.; Businger, S.; Herring, T.A.; Rocken, C.; Anthes, R.A.; Ware, R.H. GPS meteorology: Remote sensing of atmospheric water vapor using the global positioning system. *J. Geophys. Res.* **1992**, *97*, 15787. [CrossRef]
16. Houlié, N.; Briole, P.; Nercessian, A.; Murakami, M. Volcanic Plume Above Mount St. Helens Detected with GPS. *EOS Trans.* **2005**, *86*, 277–281. [CrossRef]
17. Pinto Jayawardena, T.S.; Chartier, A.T.; Spencer, P.; Mitchell, C.N. Imaging the topside ionosphere and plasmasphere with ionospheric tomography using COSMIC GPS TEC. *J. Geophys. Res. Space Phys.* **2016**, *121*, 817–831. [CrossRef]
18. Dautermann, T.; Calais, E.; Mattioli, G.S. Global Positioning System detection and energy estimation of the ionospheric wave caused by the 13 July 2003 explosion of the Soufrière Hills Volcano, Montserrat. *J. Geophys. Res.* **2009**, *114*, B02202. [CrossRef]
19. Heki, K.; Ping, J. Directivity and apparent velocity of the coseismic ionospheric disturbances observed with a dense GPS array. *Earth Planet. Sci. Lett.* **2005**, *236*, 845–855. [CrossRef]
20. Heki, K.; Otsuka, Y.; Choosakul, N.; Hemmakorn, N.; Komolmis, T.; Maruyama, T. Detection of ruptures of Andaman fault segments in the 2004 great Sumatra earthquake with coseismic ionospheric disturbances. *J. Geophys. Res.* **2006**, *111*, B09313. [CrossRef]
21. Astafyeva, E.; Rolland, L.M.; Sladen, A. Strike-slip earthquakes can also be detected in the ionosphere. *Earth Planet. Sci. Lett.* **2014**, *405*, 180–193. [CrossRef]
22. Artru, J.; Ducic, V.; Kanamori, H.; Lognonné, P.; Murakami, M. Ionospheric detection of gravity waves induced by tsunamis. *Geophys. J. Int.* **2005**, *160*, 840–848. [CrossRef]
23. Afraimovich, E.L.; Astafyeva, E.I.; Demyanov, V.V.; Edemskiy, I.K.; Gavrilyuk, N.S.; Ishin, A.B.; Kosogorov, E.A.; Leonovich, L.A.; Lesyuta, O.S.; Palamartchouk, K.S.; et al. A review of GPS/GLONASS studies of the ionospheric response to natural and anthropogenic processes and phenomena. *J. Space Weather Space Clim.* **2013**, *3*, A27. [CrossRef]
24. Jin, Y.; Zhou, X.; Moen, J.I.; Hairston, M. The auroral ionosphere TEC response to an interplanetary shock. *Geophys. Res. Lett.* **2016**, *43*, 1810–1818. [CrossRef]
25. Calais, E.; Bernard Minster, J.; Hofton, M.; Hedlin, M. Ionospheric signature of surface mine blasts from Global Positioning System measurements. *Geophys. J. Int.* **1998**, *132*, 191–202. [CrossRef]
26. Bowling, T.; Calais, E.; Haase, J.S. Detection and modelling of the ionospheric perturbation caused by a Space Shuttle launch using a network of ground-based Global Positioning System stations. *Geophys. J. Int.* **2013**, *192*, 1324–1331. [CrossRef]
27. Pichon, A.L.; Blanc, E.; Hauchecorne, A. *Infrasound Monitoring for Atmospheric Studies*; Springer: Berlin, Germany, 2010.
28. Rakoto, V.; Lognonné, P.; Rolland, L. Tsunami modeling with solid Earth–ocean–atmosphere coupled normal modes. *Geophys. J. Int.* **2017**, *211*, 1119–1138. [CrossRef]

29. Rakoto, V.; Lognonné, P.; Rolland, L.; Coïsson, P. Tsunami Wave Height Estimation from GPS-Derived Ionospheric Data. *J. Geophys. Res. Sp. Phys.* **2018**, *123*, 4329–4348. [CrossRef]
30. Afraimovich, E.L.; Perevalova, N.P.; Plotnikov, A.V.; Uralov, A.M. The shock-acoustic waves generated by earthquakes. *Ann. Geophys.* **2001**, *19*, 395–409. [CrossRef]
31. Rolland, L.M.; Vergnolle, M.; Nocquet, J.M.; Sladen, A.; Dessa, J.X.; Tavakoli, F.; Nankali, H.R.; Cappa, F. Discriminating the tectonic and non-tectonic contributions in the ionospheric signature of the 2011, M w 7.1, dip-slip Van earthquake, Eastern Turkey. *Geophys. Res. Lett.* **2013**, *40*, 2518–2522. [CrossRef]
32. Cahyadi, M.N.; Heki, K. Coseismic ionospheric disturbance of the large strike-slip earthquakes in North Sumatra in 2012: M_w dependence of the disturbance amplitudes. *Geophys. J. Int.* **2014**, *200*, 116–129. [CrossRef]
33. Rolland, L.M.; Lognonné, P.; Munekane, H. Detection and modeling of Rayleigh wave induced patterns in the ionosphere. *J. Geophys. Res. Space Phys.* **2011**, *116*, A05320. [CrossRef]
34. Occhipinti, G.; Rolland, L.; Lognonné, P.; Watada, S. From Sumatra 2004 to Tohoku-Oki 2011: The systematic GPS detection of the ionospheric signature induced by tsunamigenic earthquakes. *J. Geophys. Res. Space Phys.* **2013**, *118*, 3626–3636. [CrossRef]
35. Lee, R.F.; Rolland, L.M.; Mikesell, T.D. Seismo-Ionospheric Observations, Modeling, and Backprojection of the 2016 Kaikōura Earthquake. *Bull. Seismol. Soc. Am.* **2018**, *108*, 1794–1806. [CrossRef]
36. Thomas, D.; Bagiya, M.S.; Sunil, P.S.; Rolland, L.; Sunil, A.S.; Mikesell, T.D.; Nayak, S.; Mangalampalli, S.; Ramesh, D.S. Revelation of early detection of co-seismic ionospheric perturbations in GPS-TEC from realistic modelling approach: Case study. *Sci. Rep.* **2018**, *8*, 12105. [CrossRef]
37. Poole, A.; Sutcliffe, P. Mechanisms for observed total electron content pulsations at mid latitudes. *J. Atmos. Terr. Phys.* **1987**, *49*, 231–236. [CrossRef]
38. Heki, K. Ionospheric disturbances related to earthquakes. In *Advances In Ionospheric Research: Current Understanding and Challenges*; Huang, C., Ed.; Wiley/AGU Book: Hoboken, NJ, USA, 2019; Chapter 5-3.
39. Mannucci, A.J.; Wilson, B.D.; Yuan, D.N.; Ho, C.H.; Lindqwister, U.J.; Runge, T.F. A global mapping technique for GPS-derived ionospheric total electron content measurements. *Radio Sci.* **1998**, *33*, 565–582. [CrossRef]
40. Garner, T.; Gaussiran, T., II; Tolman, B.; Harris, R.; Calfas, R.; Gallagher, H. Total electron content measurements in ionospheric physics. *Adv. Space Res.* **2008**, *42*, 720–726. [CrossRef]
41. Bristow, K.L.; Campbell, G.S. On the relationship between incoming solar radiation and daily maximum and minimum temperature. *Agric. For. Meteorol.* **1984**, *31*, 159–166. [CrossRef]
42. Bilitza, D.; Altadill D.; Truhlik V.; Shubin V.; Galkin I.; Reinisch B.; Huang X. International Reference Ionosphere 2016: From ionospheric climate to real-time weather predictions. *Space Weather* **2017**, *15*, 418–429. [CrossRef]
43. Macleod, M.A. Sporadic E Theory. I. Collision-Geomagnetic Equilibrium. *J. Atmos. Sci.* **1966**, *23*, 96–109.<0096:SETICG>2.0.CO;2. [CrossRef]
44. Lee, R.F. Characterizing Coseismic Ionospheric Disturbance for Surface-Rupturing Earthquakes. Master's Thesis, Boise State University, Boise, ID, USA, 2017; doi:10.18122/B2WD97.
45. Gõmez, D.; Smalley, R.; Langston, C.A.; Wilson, T.J.; Bevis, M.; Dalziel, I.W.D.; Kendrick, E.C.; Konfal, S.A.; Willis, M.J.; Piñõn, D.A.; et al. Virtual array beamforming of GPS TEC observations of coseismic ionospheric disturbances near the Geomagnetic South Pole triggered by teleseismic megathrusts. *J. Geophys. Res. A Sp. Phys.* **2015**, *120*, 9087–9101. [CrossRef]
46. Thébault, E.; Finlay, C.C.; Beggan, C.D.; Alken, P.; Aubert, J.; Barrois, O.; Bertrand, F.; Bondar, T.; Boness, A.; Brocco, L.; et al. International Geomagnetic Reference Field: The 12th generation. *Earth Planets Space* **2015**, *67*, 79. [CrossRef]
47. Kherani, E.A.; Lognonné, P.; Hébert, H.; Rolland, L.; Astafyeva, E.; Occhipinti, G.; Coïsson, P.; Walwer, D.; de Paula, E.R. Modelling of the total electronic content and magnetic field anomalies generated by the 2011 Tohoku-Oki tsunami and associated acoustic-gravity waves. *Geophys. J. Int.* **2012**, *191*. [CrossRef]
48. Zettergren, M.D.; Snively, J.B. Ionospheric response to infrasonic-acoustic waves generated by natural hazard events. *J. Geophys. Res. Space Phys.* **2015**, *120*, 8002–8024. [CrossRef]
49. Zettergren, M.D.; Snively, J.B.; Komjathy, A.; Verkhoglyadova, O.P. Nonlinear ionospheric responses to large-amplitude infrasonic-acoustic waves generated by undersea earthquakes. *J. Geophys. Res. Space Phys.* **2017**, *122*, 2272–2291. [CrossRef]

50. Meng, X.; Verkhoglyadova, O.P.; Komjathy, A.; Savastano, G.; Mannucci, A.J. Physics-Based Modeling of Earthquake-Induced Ionospheric Disturbances. *J. Geophys. Res. Space Phys.* **2018**, *123*, 8021–8038. [CrossRef]
51. Dessa, J.X.; Virieux, J.; Lambotte, S. Infrasound modeling in a spherical heterogeneous atmosphere. *Geophys. Res. Lett.* **2005**, *32*, L12808. [CrossRef]
52. Matoza, R.S.; Fee, D.; Green, D.N.; Le Pichon, A.; Vergoz, J.; Haney, M.M.; Mikesell, T.D.; Franco, L.; Valderrama, O.A.; Kelley, M.R.; et al. Local, Regional, and Remote Seismo-acoustic Observations of the April 2015 VEI 4 Eruption of Calbuco Volcano, Chile. *J. Geophys. Res. Solid Earth* **2018**, *123*, 3814–3827. [CrossRef]
53. Garcia, R.; Lognonné, P.; Bonnin, X. Detecting atmospheric perturbations produced by Venus quakes. *Geophys. Res. Lett.* **2005**, *32*, 1–4. [CrossRef]
54. Lognonné, P.; Clévédé, E.; Kanamori, H. Computation of seismograms and atmospheric oscillations by normal-mode summation for a spherical earth model with realistic atmosphere. *Geophys. J. Int.* **1998**, *135*, 388–406. [CrossRef]
55. Song, X.; Zhang, Y.; Shan, X.; Liu, Y.; Gong, W.; Qu, C. Geodetic Observations of the 2018 Mw 7.5 Sulawesi Earthquake and Its Implications for the Kinematics of the Palu Fault. *Geophys. Res. Lett.* **2019**, 4212–4220. [CrossRef]
56. Bao, H.; Ampuero, J.P.; Meng, L.; Fielding, E.J.; Liang, C.; Milliner, C.W.; Feng, T.; Huang, H. Early and persistent supershear rupture of the 2018 magnitude 7.5 Palu earthquake. *Nat. Geosci.* **2019**, *12*. [CrossRef]
57. Oppenheim, A.V.; Schafer, R.W.; Buck, J.R. *Discrete-Time Signal Processing*, 2nd ed.; Prentice Hall: Upper Saddle River, NJ, USA, 1999.
58. Bagiya, M.S.; Sunil, P.S.; Sunil, A.S.; Ramesh, D.S. Coseismic Contortion and Coupled Nocturnal Ionospheric Perturbations During 2016 Kaikoura, Mw 7.8 New Zealand Earthquake. *J. Geophys. Res. Space Phys.* **2018**, *123*, 1–11. [CrossRef]
59. Picone, J.M.; Hedin, A.E.; Drob, D.P.; Aikin, A.C. NRLMSISE-00 empirical model of the atmosphere: Statistical comparisons and scientific issues. *J. Geophys. Res. Space Phys.* **2002**, *107*. [CrossRef]
60. Tapping, K.F. The 10.7 cm solar radio flux (F 10.7). *Space Weather* **2013**, *11*, 394–406. [CrossRef]
61. Drob, D.P.; Emmert, J.T.; Meriwether, J.W.; Makela, J.J.; Doornbos, E.; Conde, M.; Hernandez, G.; Noto, J.; Zawdie, K.A.; McDonald, S.E.; et al. An update to the Horizontal Wind Model (HWM): The quiet time thermosphere. *Earth Space Sci.* **2015**, *2*, 301–319. [CrossRef]
62. Bass, H.; Sutherland, L.; Piercy, J.; Evans, L. Absorption of sound by the atmosphere. In *Physical Acoustics: Principles and Methods. Volume 17 (A85-28596 12-71)*; Academic Press, Inc.: Orlando, FL, USA, 1984; Volume 17, pp. 145–232.
63. Bass, H.E.; Chambers, J.P. Absorption of sound in the Martian atmosphere. *J. Acoust. Soc. Am.* **2001**, *109*, 3069–3071. [CrossRef]
64. Landau, L.; Lifshitz, E. *Fluid Mechanics: Landau and Lifshitz: Course of Theoretical Physics*; Elsevier Science: Amsterdam, The Netherlands, 2013.